Acta Crystallographica Section A
Foundations and Advances
ISSN 2053-2733

Received 13 December 2013
Accepted 11 June 2014

Convergent-beam electron-diffraction-pattern symmetry of nanodomains in complex lead-based perovskite crystals

Kyou-Hyun Kim[a,b]‡ and Jian-Min Zuo[a,b]*

[a]Department of Materials Science and Engineering, University of Illinois at Urbana–Champaign, Urbana, Illinois 61801, USA, and [b]Frederick Seitz Materials Research Laboratory, University of Illinois at Urbana–Champaign, Urbana, Illinois 61801, USA. Correspondence e-mail: jianzuo@illinois.edu

Convergent-beam electron diffraction (CBED) recorded using nanometre-sized probes, in principle, can detect the highest symmetry in a crystal. However, symmetry reduction may occur by overlapping crystal domains along the beam direction. Thus, delineating the relationship between the recorded and the crystal symmetry is important for studying crystals with complex nanodomains. This paper reports a study of the averaged local symmetry of 71°/109° rhombohedral (R), 90° tetragonal (T) and 180° monoclinic (M) nanodomain structures. The averaged symmetry of nanodomain structures is investigated by CBED simulations using the multislice method. The simulation results show that the 71°-R, 109°-R and 90°-T nanodomain structures partially mimic the monoclinic symmetries of *Cm* and *Pm* that have been proposed by the adaptive phase model. This study is also compared to the reported experimental CBED patterns recorded from PMN-31%PT.

1. Introduction

Complex lead-based perovskites with a general formula of $(1-x)\mathrm{Pb}(B'^{+2}_{1/3}B''^{+5}_{2/3})\mathrm{O}_{3-x}\mathrm{Pb}(B'''^{+4})\mathrm{O}_3$, for example $(1-x)\mathrm{Pb}(\mathrm{Mg}_{1/3}\mathrm{Nb}_{2/3})\mathrm{O}_{3-x}\mathrm{PbTiO}_3$ (PMN-*x*PT) and $(1-x)\mathrm{Pb}(\mathrm{Zn}_{1/3}\mathrm{Nb}_{2/3})\mathrm{O}_{3-x}\mathrm{PbTiO}_3$ (PZN-*x*PT), have attracted much research interest due to the exceptional piezoelectric properties of single crystals (Park & Shrout, 1997; Park & Hackenberger, 2002). The lead-based relaxor-ferroelectric crystals are known to have three types of macroscopic symmetry of R (rhombohedral), M (monoclinic) and T (tetragonal) at room temperature dependent on composition according to X-ray and neutron diffraction (Noblanc *et al.*, 1996; Ohwa *et al.*, 2001; Noheda, 2002; Singh & Pandey, 2003; Shuvaeva *et al.*, 2005). The M symmetry includes two different space groups of *Pm* and *Cm*. Electron-microscopy observations of these crystals show very fine and complex tweed-like image contrast, whose characteristic sizes range from a few to several tens of nanometres in width (Randall & Bhalla, 1990; Viehland *et al.*, 1995; Wang *et al.*, 2006, 2008; Wang, 2006, 2007; Kim *et al.*, 2010, 2013). The tweed-like contrast has been interpreted as polarization nanodomains; the presence of nanodomains is considered to play an important role in determining the optical properties, dielectric permittivity and polarization switching in lead-based ferroelectric crystals (Park & Shrout, 1997; Wada, Park *et al.*, 1999; Wada, Suzuki *et al.*, 1999). Thus, understanding the complex nanodomain structure could provide an important clue about the mechanisms that produce the high piezoelectric responses in relaxor-based ferroelectric crystals.

Techniques such as X-ray diffraction (XRD), neutron diffraction and optical microscopy provide information about the macroscopic, or an average, symmetry by using probe sizes that are much larger than the size of nanodomains. In contrast, CBED (convergent-beam electron diffraction) is a technique for the study of local symmetry (Buxton *et al.*, 1976; Eades, 1989; Tanaka, 1994; Spence & Zuo, 1992). CBED uses a finely focused probe of a few nanometres in diameter or less. The small probe size, however, can be used to resolve the symmetry of individual nanodomains only when the electron beam propagates within the nanodomain. This is only possible along some of the crystal orientations and for sufficiently large nanodomains. Thus, the small size of nanodomains and their complex structure are significant challenges for symmetry determination by CBED (Wang *et al.*, 2006, 2008; Schierholz *et al.*, 2008; Schierholz & Fuess, 2011, 2012; Kim *et al.*, 2012). In general, symmetry reduction occurs in the recorded CBED patterns as the electron beam propagates through overlapping nanodomains.

On the other hand, the symmetry reduction over nanodomain structures has been proposed by several groups to explain the monoclinic symmetry observed in relaxor-ferroelectric crystals in the MPB (morphotropic phase boundary) region (Viehland, 2000; Jin *et al.*, 2003*a*,*b*; Wang *et*

‡ Current address: Advanced Process and Materials R&D Group, Korea Institute of Industrial Technology, Incheon 406-840, Republic of Korea.

al., 2006, 2008; Wang, 2007). In the adaptive phase model, which was originally proposed for martensitic transformation (Khachaturyan *et al.*, 1991), R or T nanodomains in the form of finely twinned structure lead to a reduced macroscopic symmetry of M from the local symmetry of R or T (Jin *et al.*, 2003*a*,*b*; Viehland, 2000). The finely twinned R or T nanodomain structures result in three types of M symmetry of M_A, M_B and M_C according to their polarization directions. The monoclinic M_A and M_B have the same space group of *Cm*, but have different polarization directions of $[uuv]$ ($u << v$) and $[uuv]$ ($u >> v$), respectively (Vanderbilt & Cohen, 2001). On the other hand, M_C has the space group of *Pm* with a polarization direction of $[u0v]$ (Vanderbilt & Cohen, 2001). M_A and M_B (*Cm*) are considered to be only associated with the R phase, while M_C (*Pm*) is considered to be associated with the T phase (Jin *et al.*, 2003*a*,*b*; Wang, 2006).

Complex lead-based perovskite crystals are also known for possessing local symmetry fluctuations (Grinberg & Rappe, 2004; Egami, 1999, 2007; Kim *et al.*, 2013). Kim *et al.* showed that the local symmetry measured by CBED using small electron probe sizes (a few nanometres) appears to be triclinic in symmetry (*P*1) (Kim *et al.*, 2012, 2013). The monoclinic *Cm*-like symmetry can only be detected by averaging over volumes of a few hundred nm^3. The measured symmetry varies spatially and it depends on the electron probe position. While symmetry variations are expected based on the complex nanodomain structure, it is not clear exactly how the nanodomains affect the recorded CBED pattern symmetry without an account of electron dynamic diffraction.

Here, we report a simulation study of the effects of different nanodomain structures on the CBED pattern symmetry. While the symmetry in complex perovskite crystals can be varied with the probe size, this study considers the case where the probe size is much smaller than the domain width, which can be achieved by electron diffraction (Schierholz *et al.*, 2008; Schierholz & Fuess, 2011; Kim *et al.*, 2012, 2013). Nanodomain structures are modeled for two types of R twin structures (71° and 109° domain structure), T twin structure (90° domain structure), and two types of M twin structures (180° domain structure). The CBED symmetry is then simulated using the multislice method (Ishizuka & Uyeda, 1977; Spence & Zuo, 1992; Cowley, 1995). We examine the symmetry of simulated CBED patterns along the major zone axes of $\langle 001\rangle_C$, $\langle 110\rangle_C$ and $\langle 111\rangle_C$ for different domain structures. Using this approach, we are able to investigate the averaged pattern symmetry for an inclined domain wall as well, which has been rarely discussed. The obtained simulation results were then compared with the adaptive monoclinic phases and the reported experimental CBED results.

2. Simulation methods

Complex lead-based relaxor-ferroelectric crystals have a general formula of $PbBO_3$. The *B* sites are occupied by different cations such as Mg^{2+}, Zn^{2+}, Nb^{5+} and Ti^{4+} (Park & Shrout, 1997). The different species on the *B* site introduce a difference in the atomic scattering factors as well as local displacements dependent on *B*-site occupation (Grinberg & Rappe, 2004). Simulations show that as long as both the occupation of the *B* sites and the local displacements are random, the pattern symmetry is preserved when the probed volume is large enough (>32 nm^3) (Kim *et al.*, 2013). Based on this, we simply modeled the nanodomains using Ti at the *B* site as in $PbTiO_3$.

For the multislice calculation, a supercell was modeled for R and T nanodomain structure using the reported crystallographic information (Singh & Pandey, 2003; Singh *et al.*, 2006; Slodczyk *et al.*, 2005). We consider a special class of nanodomain structures that are proposed in the so-called adaptive phase model (Jin *et al.*, 2003*a*,*b*; Wang, 2007). According to the adaptive phase model, the domain boundary is formed in a twin plane. There is no misfit between the crystal lattices of the twin-related nanodomains. The nanotwin structure also self-accommodates the spontaneous ferroelastic strain and minimizes the long-range stress field (Jin *et al.*, 2003*a*,*b*). For these reasons, the strain effect on the pattern symmetry is neglected here. Several supercells are constructed for the 71°-R, 109°-R, 90°-T, 180°-M (*Cm* and *Pm*) nanodomain structures. In the constructed model, the domain is about 4 nm in width. The details of modeled structures will be shown, respectively, together with the results in the next section. For the modeled supercells, CBED patterns are simulated using a probe of ∼0.2 nm in diameter. The simulated probe is placed in the middle of the nanodomain in order to obtain the highest symmetry that can be recorded in such cases. The possible incident-beam directions we considered are not exhaustive. We will show that the cases selected for study here provide a sufficient differentiation among different nanodomain models. All the electron-diffraction simulations performed here use the atomic scattering factors of Doyle & Turner (1968) and the absorption parameters of Bird & King (1990).

In this study, the direction of mirror observed in CBED patterns is often discussed. For this, we used the direction of the mirror line ($[uvw]$) while the mirror plane direction is specified by (hkl).

3. Results

3.1. Rhombohedral nanodomains

In rhombohedral symmetry, the spontaneous polarization direction (**P**) is along $[111]_R$ (the subscript 'R' denotes the rhombohedral axes). Fig. 1(*a*) shows the possible rhombohedral polar domains in the pseudo-cubic axes. We consider here the 71° and 109° domain structures, which in the adaptive phase model have the monoclinic *Cm* of M_B and M_A symmetry, respectively. As discussed earlier, M_A and M_B are defined by the polarization directions of $[uuv]$ ($u << v$) and $[uuv]$ ($u >> v$), respectively (Vanderbilt & Cohen, 2001). The 71° domain structure as shown in Fig. 1(*b*) has $(110)_C$ twin-related domains (1 and 2 as marked in Fig. 1*b*). The **P** of domains 1 and 2 is along $[111]_C$ and $[11\bar{1}]_C$, respectively. The 109° domain structure is formed with the $(001)_C$ twin

boundary as shown in Fig. 1(*c*). The **P**'s for the marked domains 1 and 2 are then along $[111]_C$ and $[\bar{1}\bar{1}1]_C$, respectively. Both the 71° and 109° domain structures possess a common mirror among the domains. The polarization direction switches within the mirror plane.

Fig. 2(*a*) shows the modeled nanotwin structure for the 71°-R domain structure. In a crystal, an R domain can be along any of the three pseudo-cubic axes. Here, we considered that the rhombohedral *c* axis ($[001]_R$) is parallel to $[001]_C$ so that the $(110)_R$ twin plane is parallel to $(110)_C$ as shown in Fig. 1(*a*). The domains 1 (**P** = $[111]_C$) and 2 (**P** = $[11\bar{1}]_C$) are represented in blue and red, respectively. In the constructed model, the domains 1 and 2 are about 4 nm in width and they stack up to about 60 nm in length along $[001]_C$. The small domain width is selected to examine the effects of multiple domains. The thickness of each layer and the number of layers do not affect the simulated pattern symmetry as long as the strain, which is size dependent, is small and neglected. The constructed nanotwin model has the head-to-tail relation for the polarization vectors as represented by the black arrows in Fig. 2(*a*) (Wang *et al.*, 2008).

For the 71°-R nanotwin structure, the domain boundary of $(110)_C$ is parallel to $[001]_C$. The $[001]_C$ pattern symmetry, therefore, displays the same pattern symmetry as the $[001]_R$ pattern symmetry when the electron probe is placed inside the domain. Because of this, the *m* symmetry along $[110]_C$ is seen in Fig. 2(*b*). The $[100]_C$ pattern symmetry is an average over $[100]_R$ and $[010]_R$. The averaged pattern symmetry then gives onefold rotation for $[100]_C$ as shown in Fig. 2(*c*). Similarly, the $[010]_C$ direction is equivalent to $[100]_C$ so that the averaged pattern symmetry gives onefold rotation as well. For $[011]_C$, the pattern is an average over $[011]_R$ and $[10\bar{1}]_R$, resulting in onefold rotation as shown in Fig. 2(*e*). The $(110)_C$ twin plane does not break the mirror element that is parallel to the beam directions of $[110]_C$ and $[111]_C$. Thus, the averaged pattern symmetry along $[110]_C$ and $[111]_C$ gives *m* as shown in Figs. 2(*e*) and 2(*f*). For the beam direction of $[1\bar{1}1]_C$, the domain wall is parallel to the beam direction so that the pattern symmetry is the same as the single R domain along $[1\bar{1}1]_R$ when the electron probe is 0.2 nm in diameter and positioned at the center of the nanodomain. As shown in Fig. 2(*g*), the pattern symmetry has the mirror line along $[121]_C$.

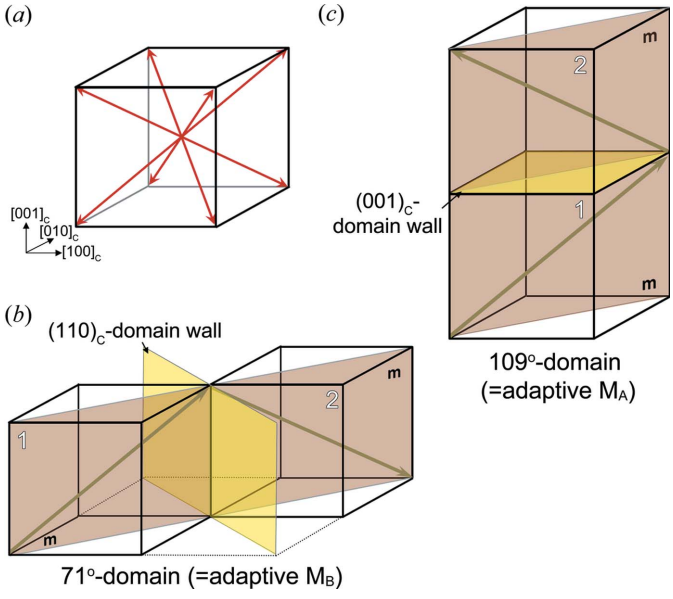

Figure 1
(*a*) Possible polarization directions of the rhombohedral domain in pseudo-cubic axes. (*b*) and (*c*) show the crystallographic orientation of the rhombohedral domain for 71° and 109° domain structure, respectively.

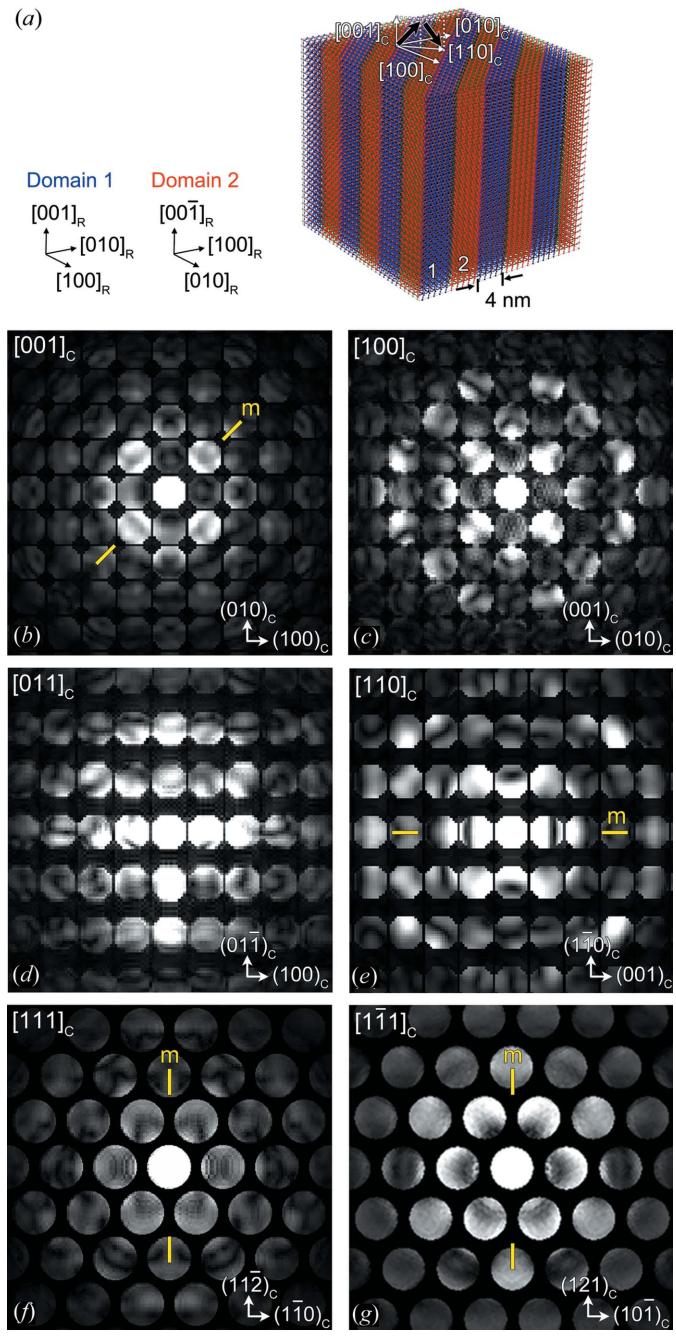

Figure 2
A model of 71°-R nanodomain structure is represented in (*a*). CBED pattern symmetry is calculated along (*b*) $[001]_C$, (*c*) $[100]_C$, (*d*) $[011]_C$, (*e*) $[110]_C$, (*f*) $[111]_C$ and (*g*) $[1\bar{1}1]_C$.

Fig. 3(*a*) shows the model for the 109°-R nanodomain structure proposed as the adaptive monoclinic phase of *Cm* (Wang, 2007). As illustrated in Fig. 1(*c*), the domains 1 and 2 are rotated by 180° about the $(001)_R$ twin plane, which corresponds to $(001)_C$. Fig. 3(*a*) provides the orientation relation for the domains 1 and 2 with respect to the pseudo-cubic axes. Then, the averaged pattern symmetry along $[001]_C$ is a result from an average over the $[001]_R$ and the 180°-rotated $[001]_R$ domain. This preserves the $(\bar{1}10)_C$ mirror plane, resulting in the averaged pattern symmetry of *m* as shown in Fig. 3(*b*). For $[100]_C$ (= $[010]_C$) and $[110]_C$, the simulated pattern symmetry is consistent with the symmetry of $[100]_R$ (Fig. 3*c*) and $[110]_R$ (Fig. 3*d*), respectively, for the reason that the beam direction is parallel to the $(001)_C$ domain boundary. The averaged symmetry along $[011]_C$ is a result of an average over the pattern symmetry of $[011]_R$ and $[0\bar{1}1]_R$. This results in onefold rotation as shown in Fig. 3(*e*). For $[111]_C$, the averaged pattern symmetry is *m* which is parallel to $[110]_C$ (Fig. 3*f*). For $[1\bar{1}1]_C$, the domain orientation is $[111]_C$ and $[\bar{1}\bar{1}1]_C$ for domains 1 and 2, respectively. The average symmetry then results in onefold rotation as shown in Fig. 3(*g*).

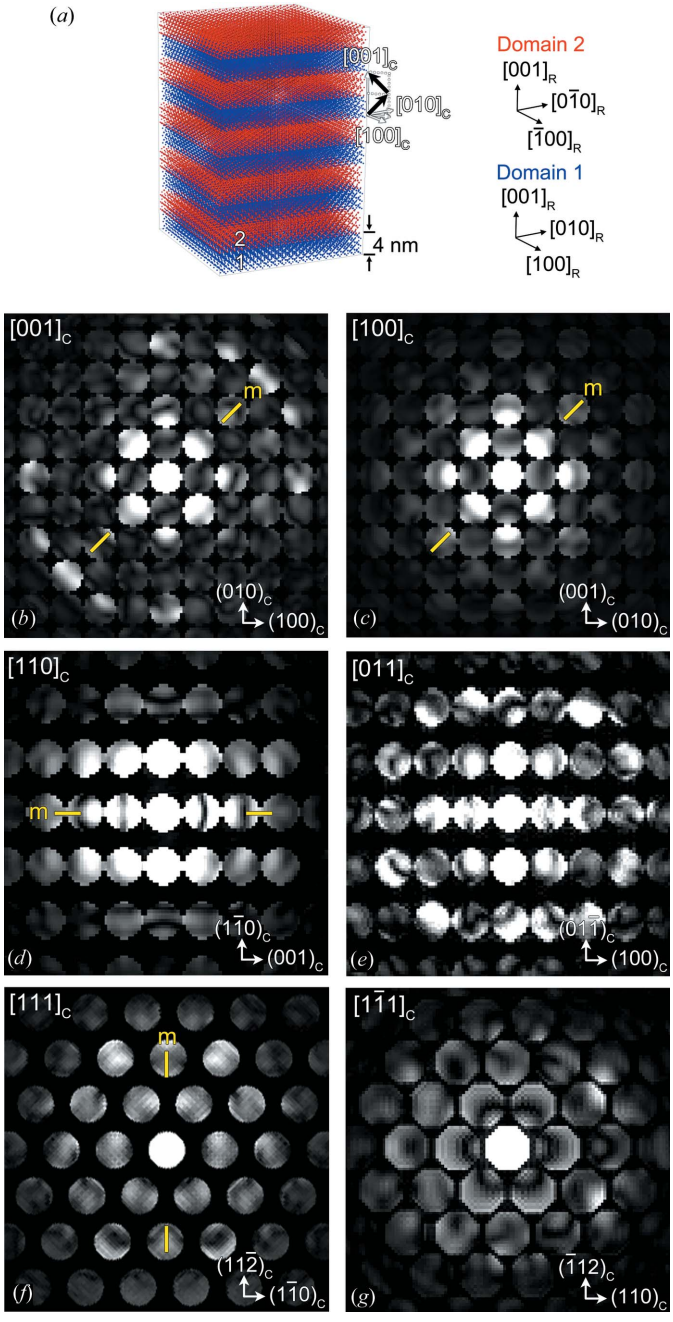

Figure 3
A model of 109°-R nanodomain structure is represented in (*a*). CBED pattern symmetry is calculated along (*b*) $[001]_C$, (*c*) $[100]_C$, (*d*) $[110]_C$, (*e*) $[011]_C$, (*f*) $[111]_C$ and (*g*) $[1\bar{1}1]_C$.

3.2. Tetragonal nanodomains

The T domain has a spontaneous polarization direction along $[001]_T$ (the subscript 'T' denotes the tetragonal axes). Fig. 4(*a*) shows the possible **P** directions in the pseudo-cubic axes. The $(101)_C$ twin-related T domain forms a 90° domain structure as shown in Fig. 4(*b*). Here, $[001]_T$ is assumed to be parallel to $[001]_C$. The domain 2 is then rotated by 90° about the domain 1, and nanodomains form the 90°-T domain structure as represented in Fig. 4(*b*). This nanodomain structure has the M_C (*Pm*) symmetry in the adaptive phase model (Jin *et al.*, 2003*a*,*b*).

Fig. 5(*a*) shows the modeled structure for 90°-T nanodomain structure. The polarization directions of domains 1 and 2 have a head-to-tail relation as marked by arrows (Jin *et al.*, 2003*a*). The pattern symmetry along $[001]_C$ is an average over $[001]_T$ and $[100]_T$. This results in *m* as shown in Fig. 5(*b*). The $[100]_C$ direction is equivalent to $[001]_C$ so that the averaged pattern symmetry also has the same symmetry of *m*. For $[010]_C$, the domain boundary is parallel to the beam direction so that the pattern symmetry is *m*, which is the pattern symmetry of $[010]_T$. For $[101]_C$, the pattern symmetry has only one mirror element (Fig. 5*d*). In $[011]_C$, the overlapped domains 1 and 2 display onefold rotation as shown in Fig. 5(*e*). The averaged symmetry along $[111]_C$ is an average over $[111]_T$ and $[\bar{1}\bar{1}\bar{1}]_T$, resulting in onefold rotation as shown in Fig. 5(*f*). For $[\bar{1}11]_C$, the pattern symmetry is the same as $[\bar{1}11]_T$ because the domain wall is parallel to the beam direction (Fig. 5*g*).

3.3. Monoclinic nanodomains

We examined monoclinic nanodomain structures based on the earlier X-ray study for PMN-*x*%PT at the MPB composition with *x* = 31% (Kim *et al.*, 2012). The reported single-

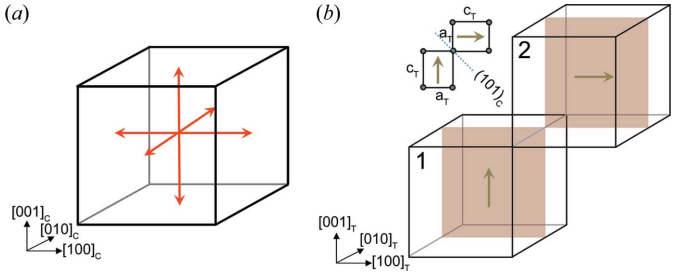

Figure 4
(*a*) Possible polarization directions of the T domain in pseudo-cubic axes. (*b*) shows the crystallographic orientation of 90°-T domain structure.

crystal XRD pattern could also be indexed with monoclinic (*Cm* and *Pm*) 180°-rotated nanodomains at the length scale of X-ray coherence (hundreds of nanometres). The polar direction of monoclinic *Cm* (M_A or M_B) and *Pm* (M_C) is $[u0v]_M$ (M_A: $u < v$, M_B: $u > v$) in the monoclinic axes (Vanderbilt & Cohen, 2001). In the pseudo-cubic axes, the polarization directions for *Cm* and *Pm* symmetry are then $[uuv]_C$ and $[u0v]_C$, respectively. CBED cannot in principle discriminate between M_A and M_B phases because two phases have the same symmetry of *Cm*. The polarization direction, therefore, was not considered for the modeled structures.

Fig. 6(*a*) shows the modeled nanodomain structure with *Cm* symmetry. The monoclinic *c* axis (c_M) lies on the pseudo-cubic axis $[001]_C$ with a small tilt of β, and a_M and b_M are rotated 45° about $[001]_C$ (Noheda, 2002; Noheda & Cox, 2006; Noheda *et al.*, 2000). Thus, a_M and b_M correspond to $[110]_C$ and $[\bar{1}10]_C$, respectively. The $[001]_C$ pattern symmetry is *m* as shown in Fig. 6(*b*). For the 180°-M (*Cm*) nanotwin structure, the domain boundary of $(001)_C$ is parallel to $[1\bar{1}0]_M$ (= $[100]_C$). The

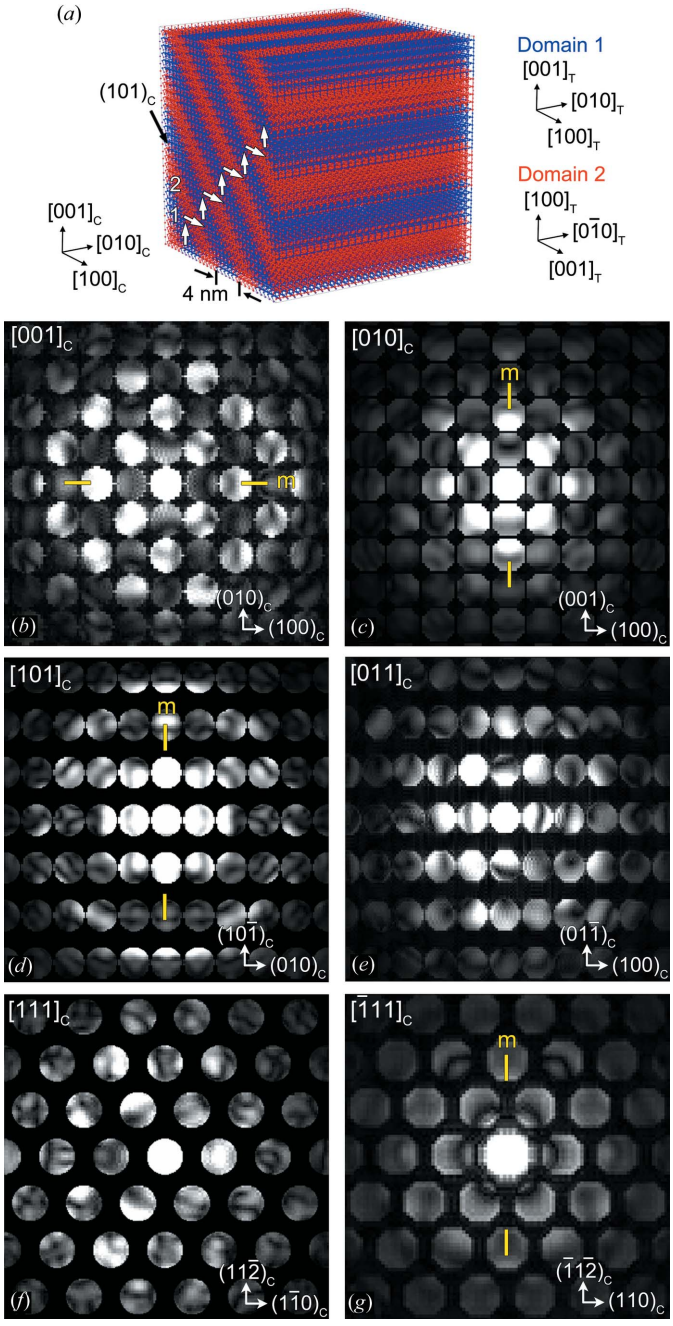

Figure 5
A model of 90°-T nanodomain structure is represented in (*a*). CBED pattern symmetry is calculated along (*b*) $[001]_C$, (*c*) $[010]_C$, (*d*) $[101]_C$, (*e*) $[011]_C$, (*f*) $[111]_C$ and (*g*) $[\bar{1}11]_C$.

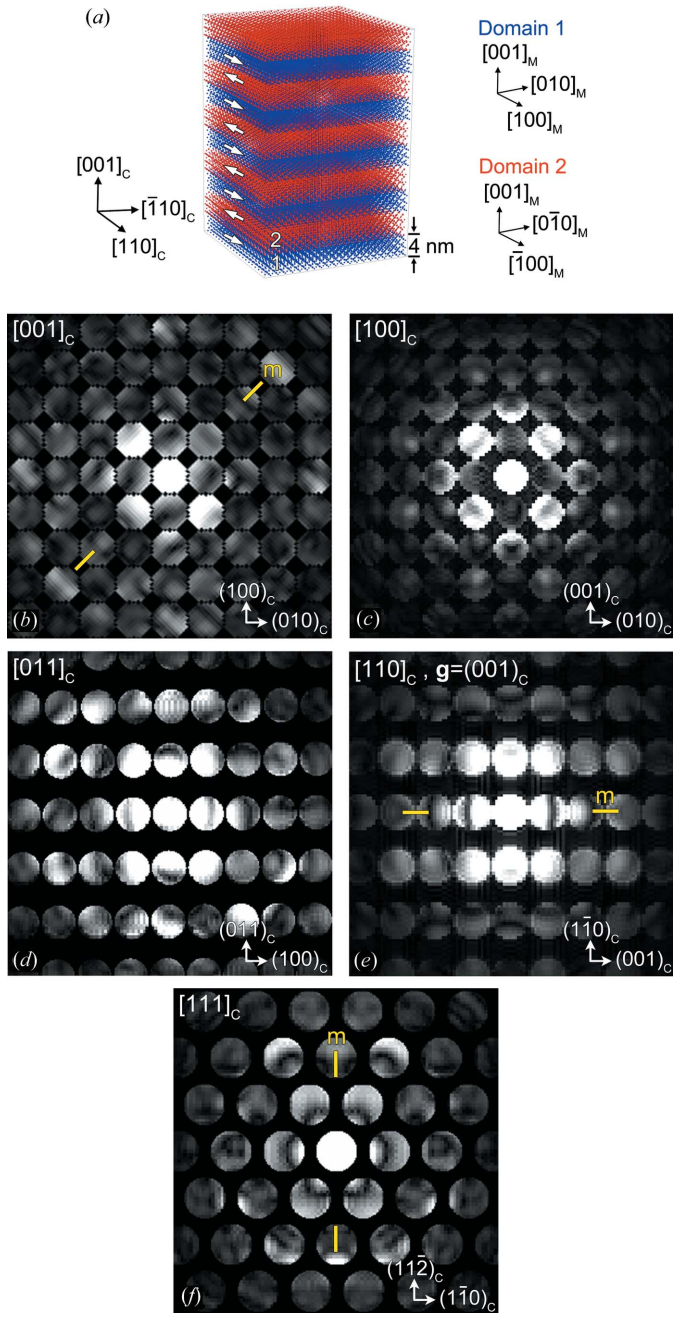

Figure 6
A model of 180°-M (*Cm*) nanodomain structure is represented in (*a*). CBED pattern symmetry for monoclinic (*Cm*) domain structure is calculated along (*b*) $[001]_C$, (*c*) $[100]_C$, (*d*) $[011]_C$, (*e*) $[110]_C$ and (*f*) $[111]_C$.

Table 1
Symmetry in the zero-order Laue zone for the monoclinic *Cm* and the R domain structures.

Here *m* stands for mirror line direction observed in the CBED pattern.

	Observing directions						
Structure	$[001]_C/[001]_M$	$[010]_C/[110]_M$	$[100]_C/[1\bar{1}0]_M$	$[110]_C/[100]_M$	$[011]_C/[112]_M$	$[1\bar{1}1]_C/[0\bar{1}1]_M$	$[111]_C/[101]_M$
Cm	$m\|[110]_C$	1	1	$m\|[001]_C$	1	1	$m\|[11\bar{2}]_C$
71°-R domain	$m\|[110]_C$†	1	1	$m\|[001]_C$	1	$m\|[112]_C$†	$m\|[11\bar{2}]_C$
109°-R domain	$m\|[110]_C$	$m\|[101]_C$†	$m\|[011]_C$†	$m\|[001]_C$†	1	1	$m\|[11\bar{2}]_C$

† These entries indicate the pattern symmetry for the zone axis parallel to the domain wall.

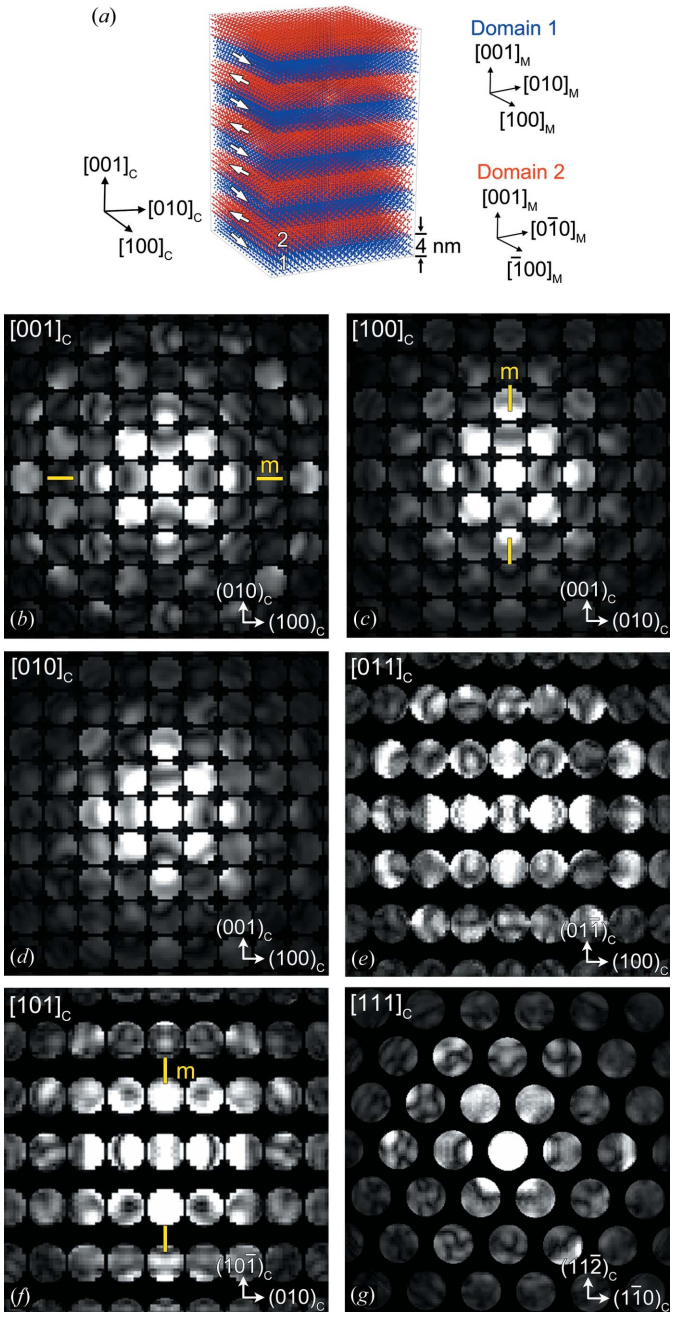

Figure 7
A model of 180°-M (*Pm*) nanodomain structure is represented in (*a*). CBED pattern symmetry for monoclinic (*Pm*) domain structure is calculated along (*b*) $[001]_C$, (*c*) $[100]_C$, (*d*) $[010]_C$, (*e*) $[011]_C$, (*f*) $[101]_C$ and (*g*) $[111]_C$.

monoclinic *Cm* structure has no mirror along $[1\bar{1}0]_M$ (= $[100]_C$) as shown in Fig. 6(*c*). For $[011]_C$, the orientation of domains 1 and 2 is $[112]_M$ and $[\bar{1}\bar{1}2]_M$. The averaged local symmetry results in no mirror as shown in Fig. 6(*d*). The $[110]_C$ pattern symmetry is parallel to a_M, resulting in *m* symmetry as shown in Fig. 6(*e*). In the zone axis of $[111]_C$, the average over the $[111]_M$ and $[\bar{1}\bar{1}1]_M$ gives *m* as shown in Fig. 6(*f*).

Similar to the 180°-M (*Cm*) nanodomain structure, the 180°-M (*Pm*) nanodomain structure is examined as shown in Fig. 7. For the monoclinic *Pm* symmetry, a_M and b_M are along $[100]_C$ and $[010]_C$. The simulations show that the averaged local symmetry has an *m* symmetry element along $[001]_C$, $[100]_C$ and $[101]_C$ as shown in Figs. 7(*b*), 7(*c*) and 7(*f*), respectively. In contrast, no symmetry is detected along the zone axes of $[010]_C$ (Fig. 7*d*), $[011]_C$ (Fig. 7*e*) and $[111]_C$ (Fig. 7*g*).

4. Discussion

Table 1 shows the averaged pattern symmetry of calculated R nanodomain structures. For comparison, the pattern symmetry expected for *Cm* is also given in Table 1. For the monoclinic M_B (*Cm*), the *c* axis (c_{M_B}) can be taken close to $[001]_C$ with a small monoclinic distortion of β, and the *a* and *b* axes (a_{M_B} and b_{M_B}) are then close to $[110]_C$ and $[\bar{1}10]_C$, respectively (Noheda, 2002; Noheda & Cox, 2006; Noheda *et al.*, 2000). Table 1 lists both the monoclinic and the pseudo-cubic axes for comparison. For the 71°-R nanodomain structure, the symmetry reduction occurs when the electron beam is not parallel to the domain wall. Nevertheless, the symmetry is not fully destroyed. The reduced symmetries along the overlapped nanodomains show the same symmetries as the monoclinic *Cm* proposed by the adaptive phase model. The 71°-R nanodomain structure, however, can be distinguished from the adaptive monoclinic *Cm* (M_B) phase by choosing the zone axis of $[1\bar{1}1]_C$. As shown in Table 1, the 71°-R nanodomain structure shows the pattern symmetry of *m* while the original *Cm* symmetry shows no symmetry. Similarly, the 109°-R nanodomain structure shows the different pattern symmetry along $[010]_C$ and $[100]_C$ from the monoclinic *Cm*.

The 90°-T domain structure is known to be associated with the monoclinic M_C (*Pm*). The c_{M_C} is almost parallel to $[001]_C$ with a small tilt of β, and the a_{M_C} and b_{M_C} lie along either $[010]_C$ or $[100]_C$. Table 2 shows the observable symmetry of monoclinic *Pm* and 90°-T domain structure along the investigated orientations. In the simulation of 90°-T nanodomain structure, a mirror symmetry is observed in both $[100]_C$ and

Table 2
Symmetry in the zero-order Laue zone for monoclinic *Pm* and the T domain structures.

	Observing directions						
Structure	$[001]_C/[001]_M$	$[010]_C/[010]_M$	$[100]_C/[100]_M$	$[101]_C/[101]_M$	$[011]_C/[011]_M$	$[111]_C/[111]_M$	$[\bar{1}11]_C/[\bar{1}11]_M$
Pm	$m\|[100]_C$	1	$m\|[001]_C$	$m\|[10\bar{1}]_C$	1	1	1
90°-domain (T)	$m\|[100]_C$	$m\|[001]_C$†	$m\|[001]_C$	$m\|[10\bar{1}]_C$	1	1	$m\|[\bar{1}1\bar{2}]_C$†

† These entries indicate the pattern symmetry for the zone axis parallel to the domain wall.

Table 3
Symmetry in the zero-order Laue zone for the monoclinic *Cm* and the *Cm* domain structure.

	Electron-beam direction					
Structure	$[001]_C/[001]_M$	$[1\bar{1}0]_M/[100]_C$	$[110]_M/[010]_C$	$[011]_C/[112]_M$	$[110]_C/[100]_M$	$[111]_C/[101]_M$
$M_{A\text{ or }B}$ (*Cm*)	$m\|[110]_C$	1	1	1	$m\|[001]_C$	$m\|[11\bar{2}]_C$
M (*Cm*) domain	$m\|[110]_C$	1†	1†	1	$m\|[001]_C$†	$m\|[11\bar{2}]_C$

† These entries indicate the pattern symmetry for the zone axis parallel to the domain wall.

Table 4
Symmetry in the zero-order Laue zone for the monoclinic *Pm* and the *Pm* domain structure.

	Electron-beam direction					
Structure	$[001]_C/[001]_M$	$[100]_C/[100]_M$	$[010]_C/[010]_M$	$[011]_C/[011]_M$	$[101]_C/[101]_M$	$[111]_C/[111]_M$
M_C (*Pm*)	$m\|[100]_C$	$m\|[001]_C$	1	1	$m\|[10\bar{1}]_C$	1
M (*Pm*) domain	$m\|[100]_C$	$m\|[001]_C$†	1†	1	$m\|[10\bar{1}]_C$†	1

† These entries indicate the pattern symmetry for the zone axis parallel to the domain wall.

$[010]_C$, while there is no mirror in the $[010]_C$ pattern symmetry of the monoclinic *Pm*.

In the case of monoclinic symmetry (Tables 3 and 4), the monoclinic nanodomain structures show the same pattern symmetry as the original structures.

The above results, obtained from twin-related nanodomains, demonstrate symmetry reduction in CBED patterns of R or T nanodomain structures except monoclinic (*Cm*, *Pm*) nanodomain structures. In all cases, the rotation symmetry expected from the parent crystal symmetry of *R*3*m* or *P*4*mm* is removed from CBED because of the nanodomain structure. Only mirror symmetry is observed when there is a common mirror plane among twin-related domains. While the averaged pattern symmetry can vary with the probe size (Schierholz *et al.*, 2008; Schierholz & Fuess, 2011; Kim *et al.*, 2012, 2013) and probe coherence, the R/T nanodomains only mimic the monoclinic *Cm* or *Pm* partially when the probe size is much smaller than the domain width.

The above simulation results then provide the map to determine the local symmetry in complex lead-based perovskite single crystals. For example, we now discuss the experimental results recently reported by Kim *et al.* on the local symmetry of PMN-31%PT (Kim *et al.*, 2012, 2013). Their study shows a probe-size-dependent symmetry; the trivial onefold rotation is detected with a 1.6 nm beam probe for the thickness of 65 nm, while approximate mirror symmetry consistent with the monoclinic *Cm* is detected when the probe size is bigger than 15 nm (Kim *et al.*, 2012, 2013). For the trivial onefold rotation symmetry, they used a probe size of 1.6 nm in diameter, which is much smaller than the nanodomain width observed in PMN-31%PT (~20 nm) (Viehland *et al.*, 1995; Wang *et al.*, 2006; Kim *et al.*, 2010, 2013). Thus, the reported experimental results can be compared to the model proposed in this study. As shown in Tables 1 and 2, the mirror symmetry element must be observed in the averaged pattern symmetry of R and T nanodomain structures. The reported experimental CBED patterns, however, show no evidence for the mirror symmetry element along $[001]_C/[010]_C/[100]_C/[011]_C/[111]_C$ with the smaller electron probe size (1.6 nm). By contrast with the probe size smaller than the domain width, the mirror symmetry is detected with a larger probe size in the same sample area (Kim *et al.*, 2012, 2013). The trivial onefold rotation in the experimental pattern, therefore, rules out the R or T symmetry inside the nanodomains in PMN-PT. Rather, all the evidence points to the monoclinic symmetry seen in X-ray and neutron diffraction and detected by CBED using probes of tens of nanometres in size, which represents a new type of symmetry where the symmetry comes from averaging over local structure (Kim *et al.*, 2013).

5. Conclusion

We have investigated the CBED symmetry of several nanodomain structures in complex lead-based ferroelectric crystals using CBED simulations. The results show that the 71°-R/109°-R/90°-T nanodomain structures can be determined by the CBED technique. The proposed nanodomain structures do not perfectly mimic the monoclinic symmetry of $M_{A\text{ or }B}$ (*Cm*) and M_C (*Pm*). Based on the simulation results, it was proven that the PMN-31%PT single crystal shows no evidence

for the R and T nanodomain structure at the local scale. By comparing the experimental and the calculation results, therefore, the lack of local symmetry observed in the experimental CBED patterns of PMN-31%PT is not a result of the R and T nanodomain structures but a result of an intrinsic structural property of the PMN-31%PT single crystal. While this study was only compared with a PMN-PT single crystal, we expect that the simulation results shown here will provide a direct method for local symmetry investigation in complex lead-based perovskite single crystals.

The work was supported by DOE BES (grant No. DEFG02-01ER45923).

References

Bird, D. M. & King, Q. A. (1990). *Acta Cryst.* A**46**, 202–208.
Buxton, B. F., Eades, J. A., Steeds, J. W. & Rackham, G. M. (1976). *Philos. Trans. R. Soc. London Ser. A*, **281**, 171–194.
Cowley, J. M. (1995). *Diffraction Physics.* Amsterdam: Elsevier.
Doyle, P. A. & Turner, P. S. (1968). *Acta Cryst.* A**24**, 390–397.
Eades, J. A. (1989). *Convergent-beam Diffraction.* New York: A. R. Liss.
Egami, T. (1999). *Ferroelectrics*, **222**, 421–428.
Egami, T. (2007). *Annu. Rev. Mater. Res.* **37**, 297–315.
Grinberg, I. & Rappe, A. M. (2004). *Phys. Rev. B*, **70**, 220101(R).
Ishizuka, K. & Uyeda, N. (1977). *Acta Cryst.* A**33**, 740–749.
Jin, Y. M., Wang, Y. U., Khachaturyan, A. G., Li, J. F. & Viehland, D. (2003*a*). *J. Appl. Phys.* **94**, 3629–3640.
Jin, Y. M., Wang, Y. U., Khachaturyan, A. G., Li, J. F. & Viehland, D. (2003*b*). *Phys. Rev. Lett.* **91**, 197601.
Khachaturyan, A. G., Shapiro, S. M. & Semenovskaya, S. (1991). *Phys. Rev. B*, **43**, 10832–10843.
Kim, K.-H., Payne, D. A. & Zuo, J.-M. (2010). *Appl. Phys. Lett.* **97**, 261910.
Kim, K.-H., Payne, D. A. & Zuo, J.-M. (2012). *Phys. Rev. B*, **86**, 184113.
Kim, K.-H., Payne, D. A. & Zuo, J. M. (2013). *J. Appl. Cryst.* **46**, 1331–1337.
Noblanc, O., Gaucher, P. & Calvarin, G. (1996). *J. Appl. Phys.* **79**, 4291–4297.
Noheda, B. (2002). *Curr. Opin. Solid State Mater. Sci.* **6**, 27–34.
Noheda, B. & Cox, D. E. (2006). *Phase Transit.* **79**, 5–20.
Noheda, B., Gonzalo, J. A., Cross, L. E., Guo, R., Park, S. E., Cox, D. E. & Shirane, G. (2000). *Phys. Rev. B*, **61**, 8687–8695.
Ohwa, H., Iwata, M., Orihara, H., Yasuda, N. & Ishibashi, Y. (2001). *J. Phys. Soc. Jpn*, **70**, 3149–3154.
Park, S.-E. & Hackenberger, W. (2002). *Curr. Opin. Solid State Mater. Sci.* **6**, 11–18.
Park, S.-E. & Shrout, T. R. (1997). *J. Appl. Phys.* **82**, 1804–1811.
Randall, C. A. & Bhalla, A. S. (1990). *Jpn. J. Appl. Phys. Part 1*, **29**, 327–333.
Schierholz, R. & Fuess, H. (2011). *Phys. Rev. B*, **84**, 064122.
Schierholz, R. & Fuess, H. (2012). *J. Appl. Cryst.* **45**, 766–777.
Schierholz, R., Fuess, H., Tsuda, K., Ogata, Y., Terauchi, M. & Theissmann, R. (2008). *Phys. Rev. B*, **78**, 024118.
Shuvaeva, V. A., Glazer, A. M. & Zekria, D. (2005). *J. Phys. Condens. Matter*, **17**, 5709–5723.
Singh, A. K. & Pandey, D. (2003). *Phys. Rev. B*, **67**, 064102.
Singh, A. K., Pandey, D. & Zaharko, O. (2006). *Phys. Rev. B*, **74**, 024101.
Slodczyk, A., Kania, A., Daniel, P. & Ratuszna, A. (2005). *J. Phys. D Appl. Phys.* **38**, 2910–2918.
Spence, J. C. H. & Zuo, J. M. (1992). *Electron Microdiffraction.* New York: Plenum Press.
Tanaka, M. (1994). *Acta Cryst.* A**50**, 261–286.
Vanderbilt, D. & Cohen, M. H. (2001). *Phys. Rev. B*, **63**, 094108.
Viehland, D. (2000). *J. Appl. Phys.* **88**, 4794–4806.
Viehland, D., Kim, M. C., Xu, Z. & Li, J. F. (1995). *Appl. Phys. Lett.* **67**, 2471–2473.
Wada, S., Park, S.-E., Cross, L. E. & Shrout, T. R. (1999). *Ferroelectrics*, **221**, 147–155.
Wada, S., Suzuki, S., Noma, T., Suzuki, T., Osada, M., Kakihana, M., Park, S. E., Cross, L. E. & Shrout, T. R. (1999). *Jpn. J. Appl. Phys. Part 1*, **38**, 5505–5511.
Wang, H., Zhu, J., Lu, N., Bokov, A. A., Ye, Z. G. & Zhang, X. W. (2006). *Appl. Phys. Lett.* **89**, 042908.
Wang, H., Zhu, J., Zhang, X. W., Tang, Y. X. & Luo, H. S. (2008). *J. Am. Ceram. Soc.* **91**, 2382–2384.
Wang, Y. U. (2006). *Phys. Rev. B*, **73**, 014113.
Wang, Y. U. (2007). *Phys. Rev. B*, **76**, 024108.